
High-Intensity Laser–Plasma Interaction with Wedge-Shaped–Cavity Targets

Introduction

The interaction of intense, picosecond laser pulses with cone- and wedge-shaped–cavity targets is an important topic for applications such as fast ignition,¹ proton^{2,3} and electron⁴ acceleration, x-ray generation,⁵ and isochoric heating⁶ of solid matter. The primary coupling mechanism of high-intensity laser pulses ($\geq 10^{18}$ W/cm²) interacting with solids is the acceleration of electrons to kinetic energies of up to several MeV. A significant portion of the laser energy is converted into these suprathermal electrons. Maximizing this conversion efficiency for the various applications is a major challenge.

A number of factors that affect the conversion efficiency include the laser contrast (which is defined as the ratio of peak power to the power of a pedestal at a certain time before the main pulse), the laser polarization, and the target geometry. Several studies have shown that a high contrast ratio is critically important for cone-in-shell fast ignition.^{7–9} A better coupling efficiency has been demonstrated with second-harmonic irradiation of microcones.¹⁰ It has also been shown that pre-plasma formation in the hollow cone substantially affects the conversion process.^{8,9} Large-scale-length plasmas inside the cone significantly influence the relativistic laser–plasma interaction, the laser-energy deposition, and the generation and transport of hot electrons toward the compressed fuel core.¹¹

The coupling efficiency in wedge and cone targets is not completely understood, and more studies are required to fully quantify how the shape of the target affects the fast-electron production for the various applications. Particle-in-cell (PIC) simulations by Nakamura *et al.*³ predicted that higher-energy fast electrons and protons would be produced using cones having a narrower (30°) cone angle and irradiated with a laser intensity of $\sim 10^{19}$ W/cm². The simulations predict that laser energy is more efficiently absorbed and funneled into the tip of the cone through surface-field effects. Similar studies were performed by Lasinski *et al.* with 2-D PIC simulations for fast-ignition targets.¹² The cone geometry was studied to maximize the laser energy that is absorbed into fast electrons and to optimize the conditions for achieving a collimated fast-

electron beam at the tip. Other theoretical studies predict some benefit of using cone-shaped targets over flat foils in terms of increased laser absorption and enhanced energy transfer into fast electrons¹³ and surface-guided fast electrons into the cone tip.¹⁴

This article presents experimental studies of fast-electron generation in hollow wedge-shaped–cavity targets, which consist of two square copper metal foils that are seamlessly joined together at one side to form a cavity. A laser beam with a contrast ratio higher than 10^8 was focused into the cavity to the target’s corner with intensities of $\sim 1 \times 10^{19}$ W/cm² using either *s*- or *p*-polarization irradiation.^{15,16} The small-mass targets were in the refluxing regime,¹⁷ meaning that strong Debye sheath fields were created at the target boundaries that confined the majority of the fast electrons in the target.¹⁸ This made it possible to infer the laser-to-fast-electron conversion efficiency by measuring the absolute K_{α} -line emission produced in the target.¹⁹ The following sections describe the targets and the experimental setup; present and analyze the experimental results; discuss the results and compare them to 2-D PIC simulations; and present conclusions of this work.

Targets and Experimental Setup

General Atomics fabricated the targets by micromachining small wedges from ~ 100 - μm -wide aluminum (Al) bars to form an extremely sharp edge (edge radius of curvature of less than ~ 1 μm); the bars were electroplated with a thin (~ 20 - μm) Cu layer on both sides and cut into separate pieces. The inner Al material was etched away, leaving hollow Cu wedges comprising two ~ 100 - μm squares of ~ 20 - μm thickness joined seamlessly together. Figure 122.9 shows photos of (a) 30°- and (b) 45°-opening-angle wedges mounted on a target stalk.

Targets with 30°, 45°, and 60° full opening angles were fabricated. The laser propagated along the *y* direction (see Fig. 122.9 for the definition of the coordinate system) into the cavity with its focal plane located at the inside wedge seam. The inside corner radius was estimated to be ~ 1 μm , smaller than the focal-spot diameter of ~ 5 μm . The wedge-shaped–cavity

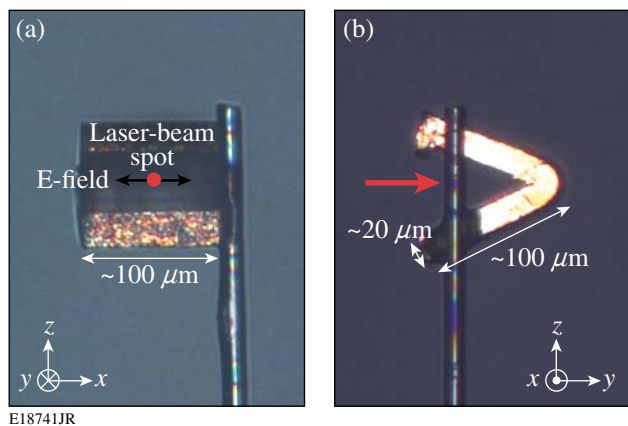


Figure 122.9

(a) A mounted 30°-opening-angle wedge looking along the laser propagation direction and (b) a mounted 45°-opening-angle wedge orthogonal to the laser propagation direction. Both targets were mounted for *s*-polarization irradiation.

targets' orientation set the laser polarization with respect to the target surface. With the electric field vector of the laser beam along the *x* direction, both targets in Fig. 122.9 were mounted for *s*-polarization irradiation. Rotating the target by 90° around the laser axis made it possible to investigate the interaction with a *p*-polarized beam. The targets were mounted onto 17- μm -diam SiC fibers. The accuracy of the target mounting with respect to beam polarization was estimated to be 5°. The targets were aligned with a precision of $\sim 5\ \mu\text{m}$ and $\sim 2^\circ$ with a target-positioning station comprising three translational and one rotational axes; a target-viewing system made two orthogonal views of the target possible. Approximately 40 targets were used in this campaign with about half for each polarization.

The Multi-Terawatt (MTW) Laser System consists of an optical parametric chirped-pulse amplification (OPCPA) front end,¹⁵ which delivered pulses with $\sim 250\text{-mJ}$ energy and 0.5-ps duration at $\lambda = 1.053\ \mu\text{m}$; these pulses were subsequently amplified in a Nd:glass amplifier chain up to 10 J (Ref. 20). For this experiment, pulse energies of around 5 J with 1-ps duration were used. The beam was focused with an off-axis parabolic mirror with an effective *f* number of ~ 4 to a nearly diffraction limited spot of $\sim 5\text{-}\mu\text{m}$ diameter, defined by the full width at half maximum (FWHM) of a peak intensity of $\sim 1 \times 10^{19}\ \text{W}/\text{cm}^2$. The high temporal contrast was measured with a scanning third-order cross correlator. The ratio of the peak power to the power of a pedestal 100 ps before the main pulse was $>10^8$ (Ref. 16).

Laser-produced fast electrons generated an 8-keV line emission by knocking out K-shell electrons. Both x rays and

energetic electrons may produce inner-shell vacancies, assuming that the radiation has sufficient energy to excite above the K edge (for Cu, $h\nu > 9\ \text{keV}$), but energetic electrons are the main contributors to K_{α} and K_{β} production in a high-intensity, ultrashort, laser–solid interaction with low- and mid-*Z* materials.²¹ Three different single-shot x-ray diagnostics measured the 8-keV K_{α} fluorescence emission from the Cu targets. A single-photon-counting x-ray spectrograph (XCCD),²² a crystal spectrograph equipped with two highly oriented pyrolytic graphite (HOPG) crystals, and a crystal imager (IMAGER)²³ were used. The IMAGER was a spherically curved α -quartz (2131) crystal with a 38-cm bending radius that imaged the $\text{K}_{\alpha 1}$ emission in a narrow spectral bandwidth of $E/\Delta E = 1340$ and $8.57\times$ magnification onto a front-illuminated, 16-bit charge-coupled-device (CCD) camera.²⁴ A 13.5- μm , 1024 \times 1024-pixel chip provided a field of view of $\sim 1.6\ \text{mm} \times 1.6\ \text{mm}$. A 1.6-cm-diam aperture in front of the crystal reduced the astigmatism, resulting in a spatial resolution of $\sim 15\ \mu\text{m}$. A thin, 35- μm Cu foil was mounted in front of the CCD camera to block stray laser light and provide bandpass filtering in the x-ray range from 8 to 9 keV. Additional lead apertures were introduced in the beam path to block the direct line of sight.

The HOPG consisted of two grade-ZYA (low-mosaic-spread) crystals,²⁵ 10 mm \times 50 mm and 2-mm thickness mounted 49 cm away from the target. The crystals covered photon-energy ranges of ~ 7.7 to $\sim 8.7\ \text{keV}$ and ~ 8.2 to $\sim 9.2\ \text{keV}$, respectively. A 16-bit, back-illuminated SI-800 CCD²⁴ with 2048 \times 2048, 13.5- μm -wide pixels was mounted 49 cm from the crystals to use mosaic focusing for best spectral resolution.²⁶ A spectral resolution of $E/\Delta E \approx 700$ was sufficient to resolve the $\text{K}_{\alpha 1}$ (8048-eV) and $\text{K}_{\alpha 2}$ (8028-eV) transitions. The integrated reflectivity of the HOPG crystal dispersing the K_{α} signal was measured with $2.82 \pm 0.1\ \text{mrad}$ at two different locations on the crystal. A 10- μm Cu foil filter mounted in front of the HOPG crystal blocked visible and soft x-ray radiation from the target while providing $>60\%$ transmission in the region of interest. Both the HOPG crystal and the XCCD used SI-800 CCD models equipped with back-illuminated chips from e2v Technologies,²⁷ comprising a 16- μm -thick depletion layer.²⁸ The XCCD's spectral resolution of $E/\Delta E \approx 45$ at 8 keV was insufficient to resolve the fine transitions. An absolute calibration was performed in Ref. 28 for single-photon-counting applications of the same camera model and chip used in this experiment. Assuming this calibration for the XCCD, an efficiency of $3.1 \pm 0.5\%$ was inferred for 8-keV x-ray photons when using the standard histogram analysis method.²⁸ This is lower than the $5 \pm 2.5\%$ that was previously measured for that camera model, but it is still in agreement with the recent calibration

within the measurement uncertainties.^{22,29} The current calibration error of the XCCD was $\sim 20\%$. An absolute calibration of the HOPG was obtained by taking into account the quantum efficiency of a $16\text{-}\mu\text{m}$ -thick Si slab at $\sim 8\text{ keV}$, the measured crystal reflectivity, the dispersion curve, and the transmission of the $10\text{-}\mu\text{m}$ Cu foil in front of the spectrograph. The HOPG calibration error was $\sim 10\%$.

The simultaneously operating diagnostics had different viewing directions: the azimuthal (θ) and polar (ϕ) diagnostic angles were $\theta = 135.0^\circ, 90.0^\circ, 62.4^\circ$ and $\phi = 0^\circ, 355.0^\circ, 59.7^\circ$ for the IMAGER, HOPG, and XCCD, with respect to the coordinate system shown in Fig. 122.9 with the polar axis along the z direction and the laser propagation along the y direction.

Experimental Results and Analysis

Figure 122.10 shows a spatially resolved K_α image of a 60° wedge. A nearly homogeneous emission was observed over the target although the laser interacted with only a small target region in the seam. The measurement indicated that the laser-generated fast electrons homogeneously filled the target. Only a small percentage of the fast electrons were energetic enough to escape the target. The resulting net charge set up strong electrostatic sheath fields at the target boundaries. Most of the fast electrons were confined in the target and were reflected back into the target upon reaching the boundary. The refluxing fast electrons eventually filled the target, provided that their mean-

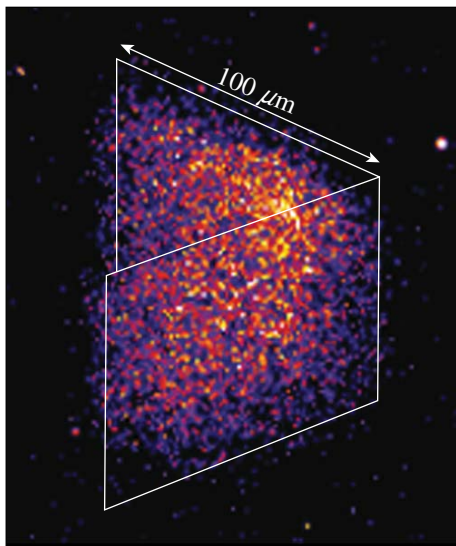


Figure 122.10 X-ray image of an s -polarized 60° -opening-angle wedge target (shot 2117). A nearly spatially homogenous 8-keV x-ray emission was observed. The pre-shot target boundaries are indicated by white lines for comparison.

free-path length was about the same as the target dimension or larger. The electron range in Cu is ~ 1 to $\sim 700\ \mu\text{m}$ for energies between 10 keV to 1 MeV (Ref. 30). Since fast electrons generate most of the K_α emission, this explains the observation of a spatially homogeneous fluorescence emission. Similar x-ray images were recorded with flat-foil targets.

Figure 122.11 shows measured x-ray spectra from (a) XCCD and (b) HOPG. The HOPG spectral resolution was high enough to resolve the $K_{\alpha 1}$ and $K_{\alpha 2}$ lines and the K_β line. Spectral integration yielded 4.38×10^{12} and 5.10×10^{11} photons into 4π steradians for K_α and K_β , respectively, for the XCCD spectrum. The HOPG spectrum yielded 4.39×10^{12} and 5.26×10^{11} photons for K_α and K_β . Both detectors were in very good agreement with respect to the total number of detected K_α and K_β photons.

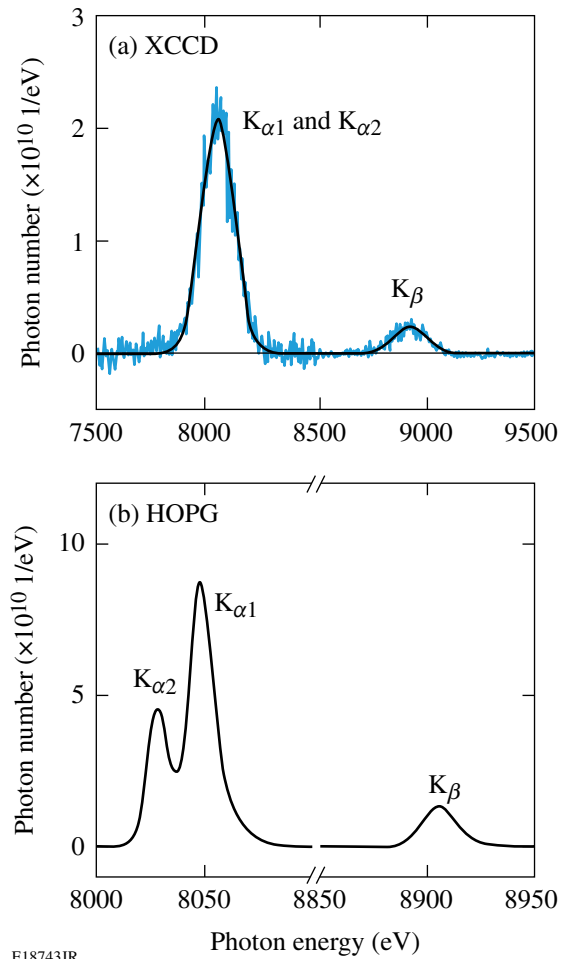


Figure 122.11 Measured x-ray spectra from XCCD (a) and HOPG (b) from a 30° -wedge target irradiated with p -polarization (shot 2164). HOPG resolved the $K_{\alpha 1}$ and $K_{\alpha 2}$ lines because of a higher spectral resolution. The abscissa is broken in (b) to show the K_α and K_β lines with reasonable resolution.

The diagnostics measured the x-ray emission from different angles with respect to the target. The line emission generated in deeper layers of the target was affected by reabsorption. This was taken into account by calculating the opacity effect for each diagnostic depending on the diagnostic view angle. The $1/e$ absorption lengths³¹ of K_α and K_β photons were $22.2 \mu\text{m}$ and $29.7 \mu\text{m}$, respectively, for the solid-state Cu material, and there was a significant direction-dependent reabsorption of that emission in the $\sim 100 \times 100 \times 40\text{-}\mu\text{m}^3$ target volume. The opacity was taken into account by describing the wedges as two rectangular prisms. $N = 2.7 \times 10^4$ grid points were placed in each prism. The average transmitted radiation

$$1/N \sum_{i=1}^N \exp(-\alpha_x d_i)$$

was calculated, where α_x was the corresponding absorption length and d_i was the distance that the radiation had to propagate through the target into the solid angle of the diagnostic. The distances depend on each grid point, the target orientation, and the diagnostic angle. The average emission from each prism was calculated, and the total emission was calculated by taking into account the partial obscuration of the radiation of one prism by the other.

Five to six laser shots were performed for each target species and polarization, and the average K_α signal was calculated. Figure 122.12 shows the measured K_α signal normalized to the laser energy as a function of the wedge angle for the different diagnostics. All three diagnostics were in good agree-

ment, showing that the Cu K_α emission was isotropic within the probed line of sights and the measurement accuracy. The open symbols represent the HOPG measurement while the solid symbols show the XCCD yields in Fig. 122.12(a) and the IMAGER yields in Fig. 122.12(b). The error bars indicate the statistical error of each measurement. The HOPG and XCCD diagnostics were absolutely calibrated, while the IMAGER was cross calibrated against the HOPG diagnostic. The data point at 180° marks the reference measurement with flat foils irradiated under normal incidence. The measured average yield of ~ 20 planar-foil targets of about the same mass was $(7.07 \pm 0.3) \times 10^{-4}$ (XCCD) and $(7.14 \pm 0.5) \times 10^{-4}$ (HOPG). The yield was a factor of 2 higher for the wedges reaching $(1.38 \pm 0.10) \times 10^{-3}$ (XCCD) and $(1.34 \pm 0.09) \times 10^{-3}$ (HOPG) for p -polarization. The data may indicate a slight increase in signal for smaller wedge angles.

Using targets that were in the refluxing regime made it possible to infer the fast-electron coupling efficiency (CE) from an absolute measurement of the K_α emission.^{18,19,22} Reference 18 describes the model that was used to infer CE from the K_α yield. The data from the three diagnostics were averaged and used to infer CE using a fixed laser intensity of $1 \times 10^{19} \text{ W/cm}^2$. The Cu inner-shell line emission depended weakly on the laser intensity in the range of 1×10^{18} to 10^{20} W/cm^2 (Refs. 19 and 22), so that intensity variations were not significant. Figure 122.13(a) shows the experimental CE for the wedge-shaped-cavity targets and for flat foils. The square symbols refer to p -polarization and the triangles show the efficiency of s -polarization. A p -polarized laser beam interacting with a narrow cavity converted significantly more short-pulse

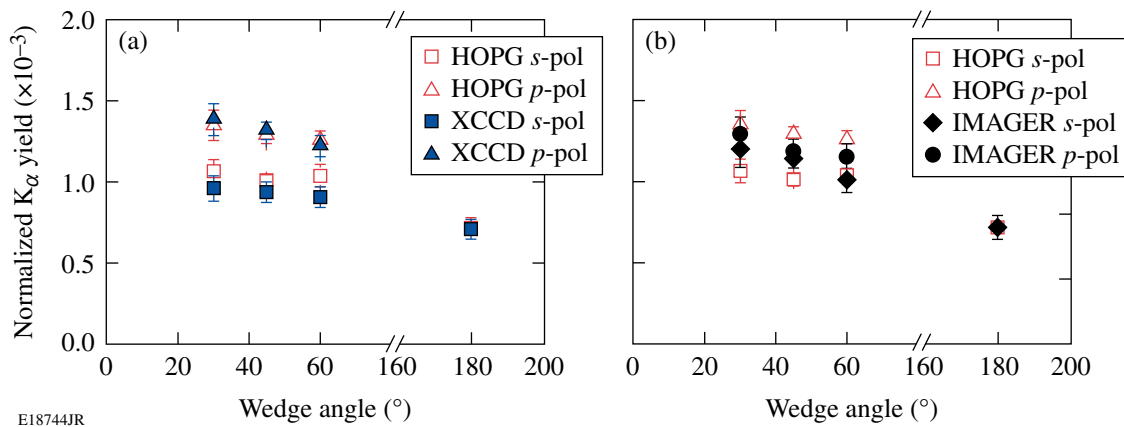


Figure 122.12 Measured K_α yield normalized to the laser energy on target from different diagnostics: (a) HOPG (open) and XCCD (solid) and (b) HOPG (open) and IMAGER (solid).

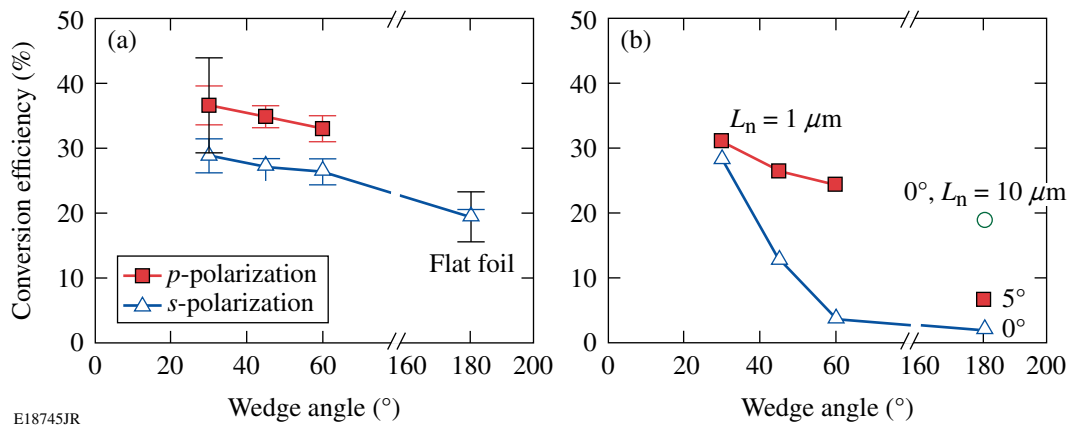


Figure 122.13

(a) Experimental and (b) theoretical conversion efficiency of short-pulse laser energy into fast electrons. The two error bars at 30° and 180° in (a) are representative absolute error bars of the measured conversion efficiency. The green circle in (b) represents a planar target with an overall target tilt of 5° relative to the beam axis. The red square at 180° in (b) was calculated using $L_n = 10 \mu\text{m}$, rather than $1 \mu\text{m}$.

energy (up to ~36%) into fast electrons than a flat foil of similar mass (20%). The absolute uncertainty of the conversion efficiency, ΔCE , was estimated at 20% relative to the CE, which gave an absolute ΔCE between $\pm 4\%$ and $\pm 7\%$ based on the calibration errors of the diagnostics. Two representative absolute error bars at 30° and 180° are included in Fig. 122.13(a).

2-D PIC Simulations and Discussion

To elucidate on the absorption mechanism, 2-D PIC simulations were performed with the code OSIRIS.³² The theoretical CE is defined as the fraction of the calculated total kinetic energy of all the electrons above 9 keV to the total laser energy. Only electrons with kinetic energy above 9 keV can contribute to the K_α production in the Cu target since the binding energy for K-shell electrons is approximately 9 keV. The calculated absorption fraction taking all the electrons into account was significantly higher. Wedge-shaped-cavity targets of 30°, 45°, and 60° full opening angle were used in the calculations, assuming a fully ionized Cu target with an electron density of $10\times$ the nonrelativistic critical electron density n_c . The initial target temperature was set to room temperature (~ 0.1 eV). The plasma density ramped linearly from zero to peak density over a $1\text{-}\mu\text{m}$ distance at the target boundary. Some simulations were performed for different density scale lengths. The simulation box of $\sim 10 \times 14 \mu\text{m}$ was divided into 600×900 cells giving a spatial resolution of $0.1 c/\omega_1 = 0.016 \mu\text{m}$, where ω_1 is the laser frequency and c is the speed of light in vacuum. There were 49 particles of each species per cell. The boundary condition in the longitudinal direction that coincides with the laser propagation direction was thermal for particles and open for the electromagnetic field. Periodic boundary conditions for

both particles and fields were chosen in the transverse direction. The $1\text{-}\mu\text{m}$ -wavelength laser pulse propagated along the symmetry axis of the cavity and was focused into the vertex to an intensity of $1 \times 10^{19} \text{ W/cm}^2$. Gaussian profiles were assumed both in time and space with a 0.5-ps (FWHM) pulse duration and a $4\text{-}\mu\text{m}$ (FWHM) focal spot.

The square and triangle symbols in Fig. 122.13(b) represent the calculations for p - and s -polarization, respectively. The calculated conversion efficiency for p -polarization slightly increased with narrower angle and reached up to 30%. Within the calibration error, simulations and experiments were in agreement for p -polarization. The PIC code showed reasonable agreement with experiment for 30° and s -polarization but calculated significantly less absorption for larger angles. The calculated strong dependence on opening angle for s -polarization was not observed in the measurement. This discrepancy may be due to imperfect polarization in the experiment. Target-alignment errors were of the order of $\sim 5^\circ$, and microstructures observed on the target surface under a light microscope might have affected the interaction. Both effects probably contributed partially p -polarized laser light. The PIC simulations calculated only 2% absorption for flat foils under normal incidence, which is much lower than measured in the experiment ($\sim 20\%$). The theoretical CE increased to 7% when the foil was tilted by 5° in the plane of incidence [see the red square at 180° in Fig. 122.13(b)]. The plasma density scale length also has a strong effect on the absorption fraction. The calculated absorption increased to 20% assuming a $10\text{-}\mu\text{m}$ density ramp on the boundary of a flat target for normal incidence [see the green circle in Fig. 122.13(b)]. Target alignment

errors, target microstructures, and density scale length have a significant effect on CE, which could explain the discrepancy of the calculated and measured absorption for flat foils.

The principal laser-absorption mechanisms responsible for the production of suprathermal electrons in this experiment are the Brunel effect,³³ resonance absorption,³⁴ and $\mathbf{j} \times \mathbf{B}$ heating.³⁵ The Brunel mechanism, or vacuum heating, describes the process when electrons are dragged out of the target surface into the vacuum by strong p -polarized fields and accelerated back into the overdense plasma, where the electrons deposit their kinetic energy. This mechanism probably explains the measured increased absorption for p -polarization. It does not, however, explain why for s -polarization the absorption in narrow cavities was larger than for flat foils that were irradiated under normal incidence. This effect was probably due to the target geometry. Despite the tight focus, the majority of the laser beam interacted with a flat target surface at a large angle of incidence. The laser absorption of obliquely irradiated flat foils generally decreases with larger angle of incidence,³⁶ while here maximum absorption was measured for the narrowest wedge cavity with a corresponding angle of incidence of 75° . The light that is reflected from one surface reaches the opposite target surface where it has another chance to be absorbed. The narrower the cavity, the more reflections the light undergoes so that the overall absorption increases, although the absorption per reflection is small due to the shallow interaction angle. A narrow wedge with reflecting walls forms a cavity where the laser field reflects multiple times between opposite walls before reaching the tip. Interference of the electromagnetic field in the vicinity of the tip then leads to a standing wave pattern that might result in higher laser intensities than for comparable laser irradiation onto a flat target at normal incidence.

Lasinski *et al.* reported 2-D PIC simulations with flat-top cones and wedge-shaped-cavity targets¹² under similar conditions ($1\text{-}\mu\text{m}$ wavelength, intensity of 1×10^{19} W/cm²). Compared to simple slab interactions, cone targets resulted in increased laser light absorption and higher temperatures of the fast-electron population, which is in general agreement with the PIC simulations shown in this article. Higher absorption was calculated for p -polarized laser light in agreement with the results presented here. The absorption reached up to 75%, which was defined in Ref. 12 as the total kinetic energy in all the electrons divided by the total light energy that had entered the simulation. The absorption fraction in this work reached $\sim 70\%$ when all the electrons were taken into account.

The ions were kept immobile in most of the simulation runs, but some runs were performed with mobile ions. No significant difference in absorption and fast-electron energy distribution was observed between fixed- and mobile-ion runs. This is similar to simulations in Ref. 12 with mobile and fixed ions that produced no significant difference in absorption and heated-electron-density distribution for a 26° full opening angle wedge cavity. In contrast, mobile ion runs for flat foils and flattop cones calculated significantly more absorption than with immobile ions. In these target geometries, the deformation of the relativistic critical-density surface by ponderomotive effects is important, especially for flat foils irradiated under normal incidence and for cones with a central flattop portion. Rippling of the plasma surface leads to an enhanced absorption through the Brunel effect³³ and resonance absorption.³⁴ The relativistic critical surface deformation is less important for wedge cavities (or cones with pointed tips) since the laser is very efficiently absorbed along the upper side walls of the target, showing insignificant difference in mobile- and fixed-ion runs.

Conclusions

High-intensity laser-plasma interaction experiments were performed with wedge-shaped-cavity Cu targets with various opening angles at a laser intensity of 1×10^{19} W/cm². Absolute measurements with three independent diagnostics viewing the target from different observation locations provided spatially and spectrally resolved measurements of the $\sim 8\text{-keV}$ K_α emission from these targets. The diagnostics measured an isotropic emission. The coupling efficiency of short-pulse laser energy into fast electrons with kinetic energy >9 keV was inferred for wedge opening angles between 30° and 60° and for s - and p -polarized laser light irradiation. An increased coupling efficiency of up to 36% was measured for the narrowest wedge and for p -polarization compared to 20% for flat foils. The experimental results are in reasonable agreement with predictions from 2-D PIC simulations for p -polarized laser light and for the narrowest cavity for s -polarization. For s -polarization and wider cavities, the calculated absorption is significantly lower than in the experiment.

ACKNOWLEDGMENT

The authors are indebted to the Target Fabrication Groups at General Atomics and LLE and to C. Mileham for experimental support. This work was supported by the U.S. Department of Energy Office of Inertial Confinement Fusion under Cooperative Agreement No. DE-FC52-08NA28302, the OFES Fusion Science Center grant No. DE-FC02-04ER54789, the OFES ACE grant No. DE-FG02-05ER54839, the University of Rochester, and the New York State Energy Research and Development Authority. The support of DOE does not constitute an endorsement by DOE of the views expressed in this article.

REFERENCES

1. M. Tabak *et al.*, *Phys. Plasmas* **1**, 1626 (1994).
2. K. A. Flippo *et al.*, *Phys. Plasmas* **15**, 056709 (2008).
3. T. Nakamura *et al.*, *Phys. Plasmas* **14**, 103105 (2007).
4. N. Renard-Le Galloudec *et al.*, *Phys. Rev. Lett.* **102**, 205003 (2009).
5. B. I. Cho *et al.*, *Phys. Plasmas* **15**, 052701 (2008).
6. P. M. Nilson, W. Theobald, J. F. Myatt, C. Stoeckl, M. Storm, J. D. Zuegel, R. Betti, D. D. Meyerhofer, and T. C. Sangster, *Phys. Rev. E* **79**, 016406 (2009).
7. L. Van Woerkom *et al.*, *Phys. Plasmas* **15**, 056304 (2008).
8. J. A. King, K. U. Akli, R. R. Freeman, J. Green, S. P. Hatchett, D. Hey, P. Jaanimagi, M. H. Key, J. Koch, K. L. Lancaster, T. Ma, A. J. MacKinnon, A. MacPhee, P. A. Norreys, P. K. Patel, T. Phillips, R. B. Stephens, W. Theobald, R. P. J. Town, L. Van Woerkom, B. Zhang, and F. N. Beg, *Phys. Plasmas* **16**, 020701 (2009).
9. S. D. Baton *et al.*, *Phys. Plasmas* **15**, 042706 (2008).
10. J. Rassuchine *et al.*, *Phys. Rev. E* **79**, 036408 (2009).
11. F. Beg, *Bull. Am. Phys. Soc.* **54**, 299 (2009); A. G. MacPhee *et al.*, *Phys. Rev. Lett.* **104**, 055002 (2010).
12. B. F. Lasinski, *Phys. Plasmas* **16**, 012705 (2009).
13. Y. Sentoku *et al.*, *Phys. Plasmas* **11**, 3083 (2004).
14. T. Nakamura *et al.*, *Phys. Rev. Lett.* **93**, 265002 (2004).
15. V. Bagnoud, I. A. Begishev, M. J. Guardalben, J. Puth, and J. D. Zuegel, *Opt. Lett.* **30**, 1843 (2005).
16. C. Dorrer, A. V. Okishev, I. A. Begishev, J. D. Zuegel, V. I. Smirnov, and L. B. Glebov, *Opt. Lett.* **32**, 2378 (2007).
17. A. J. MacKinnon *et al.*, *Phys. Rev. Lett.* **88**, 215006 (2002).
18. J. Myatt, W. Theobald, J. A. Delettrez, C. Stoeckl, M. Storm, T. C. Sangster, A. V. Maximov, and R. W. Short, *Phys. Plasmas* **14**, 056301 (2007).
19. P. M. Nilson, W. Theobald, J. Myatt, C. Stoeckl, M. Storm, O. V. Gotchev, J. D. Zuegel, R. Betti, D. D. Meyerhofer, and T. C. Sangster, *Phys. Plasmas* **15**, 056308 (2008).
20. J. D. Zuegel, V. Bagnoud, I. A. Begishev, M. J. Guardalben, J. Keegan, J. Puth, and L. J. Waxer, presented at the Conference on Lasers and Electro Optics (CLEO 2003), Baltimore, MD, 1–6 June 2003 (Paper CME3).
21. H. Chen, B. Soom, B. Yaakobi, S. Uchida, and D. D. Meyerhofer, *Phys. Rev. Lett.* **70**, 3431 (1993).
22. W. Theobald, K. Akli, R. Clarke, J. Delettrez, R. R. Freeman, S. Glenzer, J. Green, G. Gregori, R. Heathcote, N. Izumi, J. A. King, J. A. Koch, J. Kuba, K. Lancaster, A. J. MacKinnon, M. Key, C. Mileham, J. Myatt, D. Neely, P. A. Norreys, H.-S. Park, J. Pasley, P. Patel, S. P. Regan, H. Sawada, R. Shepherd, R. Snavelly, R. B. Stephens, C. Stoeckl, M. Storm, B. Zhang, and T. C. Sangster, *Phys. Plasmas* **13**, 043102 (2006).
23. K. U. Akli, M. H. Key, H. K. Chung, S. B. Hansen, R. R. Freeman, M. H. Chen, G. Gregori, S. Hatchett, D. Hey, N. Izumi, J. King, J. Kuba, P. Norreys, A. J. MacKinnon, C. D. Murphy, R. Snavelly, R. B. Stephens, C. Stoeckel, W. Theobald, and B. Zhang, *Phys. Plasmas* **14**, 023102 (2007).
24. Spectral Instruments, Tucson, AZ 85745 (http://www.specinst.com/Products/800s_datasheet.pdf).
25. Momentive Performance Materials, Albany, NY 12211 (<http://www.momentive.com/momentiveInternetDoc/Internet/Static%20Files/Documents/4%20Color%20Brochures/85508.pdf>).
26. B. Yaakobi and A. J. Burek, *IEEE J. Quantum Electron.* **QE-19**, 1841 (1983).
27. CCD42–40 Ceramic AIMO Back Illuminated Compact Package High Performance CCD Sensor, e2v technologies (uk) limited, Chelmsford, Essex CM1 2QU, UK.
28. B. R. Maddox *et al.*, *Rev. Sci. Instrum.* **79**, 10E924 (2008).
29. H.-S. Park, D. M. Chambers, H.-K. Chung, R. J. Clarke, R. Eagleton, E. Giraldez, T. Goldsack, R. Heathcote, N. Izumi, M. H. Key, J. A. King, J. A. Koch, O. L. Landen, A. Nikroo, P. K. Patel, D. F. Price, B. A. Remington, H. F. Robey, R. A. Snavelly, D. A. Steinman, R. B. Stephens, C. Stoeckl, M. Storm, M. Tabak, W. Theobald, R. P. J. Town, J. E. Wickersham, and B. B. Zhang, *Phys. Plasmas* **13**, 056309 (2006).
30. M. J. Berger, in *Methods in Computational Physics: Advances in Research and Applications*, edited by B. Alder, S. Fernbach, and M. Rotenberg, Volume 1: Statistical Physics (Academic Press, New York, 1963), pp. 135–215.
31. B. L. Henke, E. M. Gullikson, and J. C. Davis, *At. Data Nucl. Data Tables* **54**, 181 (1993).
32. R. A. Fonseca *et al.*, in *Computational Science—ICCS 2002*, edited by P. M. A. Sloot *et al.*, Lecture Notes in Computer Science (Springer, Berlin, 2002), Vol. 2331, pp. 342–351.
33. F. Brunel, *Phys. Rev. Lett.* **59**, 52 (1987).
34. P. Gibbon and A. R. Bell, *Phys. Rev. Lett.* **68**, 1535 (1992).
35. S. C. Wilks and W. L. Kruer, *IEEE J. Quantum Electron.* **33**, 1954 (1997).
36. T. Feurer, W. Theobald, R. Sauerbrey, I. Uschmann, D. Altenbernd, U. Teubner, P. Gibbon, E. Förster, G. Malka, and J. L. Miquel, *Phys. Rev. E* **56**, 4608 (1997).